

PAPER • OPEN ACCESS

## Plasma filaments in the scrape-off layer of Wendelstein 7-X

To cite this article: Carsten Killer *et al* 2020 *Plasma Phys. Control. Fusion* **62** 085003

View the [article online](#) for updates and enhancements.

### You may also like

- [The Set of Diagnostics for the First Operation Campaign of the Wendelstein 7-X Stellarator](#)  
Ralf König, J. Baldzuhn, W. Biel *et al.*
- [Features of near and far scrape-off layer heat fluxes on the Wendelstein 7-X inboard limiters](#)  
H. Niemann, M.W. Jakubowski, F. Effenberg *et al.*
- [The effects of non-uniform drive on plasma filaments](#)  
Brendan Shanahan, Ben Dudson and Peter Hill

### Recent citations

- [Slab-geometry surface waves on steep gradients and the origin of related numerical issues in a variety of ICRF codes](#)  
Wouter Tierens and Laurent Colas
- [Dynamics and Dependencies of the Configuration-Dependent 1-2 kHz Fluctuation in W7-X](#)  
S.B. Ballinger *et al*
- [Statistical characteristics of the SOL turbulence in the first divertor plasma operation of W7-X using a reciprocating probe](#)  
S. C. Liu *et al*



**IOP | ebooks™**

Bringing together innovative digital publishing with leading authors from the global scientific community.

Start exploring the collection—download the first chapter of every title for free.

# Plasma filaments in the scrape-off layer of Wendelstein 7-X

Carsten Killer<sup>1,5</sup> , Brendan Shanahan<sup>1,5</sup> , Olaf Grulke<sup>1,2</sup>, Michael Endler<sup>1</sup> , Kenneth Hammond<sup>3</sup> , Lukas Rudischhauser<sup>1</sup>  and W7-X Team<sup>4</sup>

<sup>1</sup> Max-Planck-Institut für Plasmaphysik, Wendelsteinstr. 1, 17491 Greifswald, Deutschland

<sup>2</sup> Department of Physics, Technical University of Denmark, Lyngby, Denmark

<sup>3</sup> Princeton Plasma Physics Laboratory, Princeton, NJ, United States of America

<sup>4</sup> see T Klinger, Nucl. Fusion 59 (2019) 112 004

<sup>5</sup> These authors contributed equally

Received 11 February 2020, revised 7 April 2020

Accepted for publication 14 May 2020

Published 22 June 2020



CrossMark

## Abstract

Plasma filaments have been observed by reciprocating electric probes in the Scrape-Off Layer (SOL) of the Wendelstein 7-X stellarator. Comparison with target probes indicates that a filament observed in the W7-X SOL extends to the sheath. Two-dimensional simulations of seeded filaments exhibit good quantitative agreement with experimental measurements in filament velocity scalings, despite an assumption of constant field line curvature. Both experiment and simulation show a slow radial propagation of filaments, indicating that filaments are essentially bound to their flux surface and do not perform ballistic radial motion. In contrast, the poloidal propagation along flux surfaces is much faster than the radial motion.

Keywords: plasma filament, scrape-off layer, Wendelstein 7-X, Langmuir probe, fluid model

(Some figures may appear in colour only in the online journal)

## 1. Introduction

Large, coherent, field-aligned plasma filaments are a considerable source of particle transport in the Scrape-Off Layer (SOL) of tokamaks [1–5]. Typically, such turbulent structures—also called blobs—are observed to be generated close to the separatrix, from where they ballistically move radially across the SOL, carrying heat and particles and resulting in *turbulence spreading* into the far SOL [6]. However, they are not a phenomenon exclusive to tokamaks [7–11]. The universal underlying feature is the charge separation of a positive density perturbation under the action of a polarizing force (e.g. curvature drift in toroidal magnetized plasmas), which leads to a perpendicular  $E \times B$  motion of the turbulent structure. Based on the parallel closure of the currents associated with the filament, different transport regimes can be identified. In addition to the fundamental sheath-limited and inertial (high collisionality)

regime, the magnetic shear associated with X-points in diverted tokamaks can play a major role, as it results in a significant elliptical deformation of the filament cross section [1, 12, 13].

In the Wendelstein 7-X (W7-X) stellarator, first observations of filaments in the SOL have been reported using video cameras and an Alkali metal beam emission spectroscopy [14, 15], but fundamental questions on their origin and properties remain as yet unresolved. Understanding filaments in W7-X is particularly challenging due to the complex three-dimensional geometry of the magnetic field [16] and complicated magnetic topology of the island divertor [17]. In particular, the normal magnetic curvature varies greatly along field lines and the multiple X-points result in significant magnetic shear. This novel environment for filament physics is just starting to be addressed numerically [18]. Recent numerical studies have indicated that filaments can exist even in cases of non-uniform curvature drive as long as the field-line averaged curvature is negative, i.e. interchange-unstable [19]. It is also concluded in [19] that in cases of moderate non-uniform curvature drive, filament propagation is nearly identical to scenarios with constant curvature drive, motivating the drift-plane approximation used in this work. Furthermore, previous



Original Content from this work may be used under the terms of the [Creative Commons Attribution 4.0 licence](https://creativecommons.org/licenses/by/4.0/). Any further distribution of this work must maintain attribution to the author(s) and the title of the work, journal citation and DOI.

work [11] has indicated that it is more appropriate to use the average field line curvature to determine the areas of filament generation.

Here, we present for the first time experimental observations of plasma filaments in the SOL of W7-X using Langmuir probes. The measurements are located outside of magnetic islands in order to ease interpretation by avoiding the additional complexity of island-related plasma dynamics [15, 20]. Using conditional averaging of ion saturation current and floating potential fluctuations, large scale turbulent structures are clearly identified as positive density perturbations with a poloidal electric field that leads to a radially outwards directed  $E \times B$  drift [1]. The filamentary nature of the measured structures is demonstrated by the correlation of plasma fluctuations along the local magnetic field. Scalings of filament velocity vs. size are compiled from a wide range of experimental parameters and are compared to simulations of seeded filaments in drift-plane geometry, yielding remarkable agreement.

## 2. Methods

### 2.1. Reciprocating probe measurements

Experiments were performed in a magnetic configuration of W7-X where the island divertor is formed by a  $m/n = 5/6$  island chain (*Low Iota*). In this configuration, the reciprocating probes mounted on the Multi-Purpose Manipulator (MPM) [20] are located outside the island chain but relatively close to one of the six X-points, in a region similar to the private flux region in tokamaks [21]. The path of the reciprocating probe head is indicated by the white dashed line in figure 1 with the connection lengths  $L_{\parallel}$  from the probe path to the divertor further illustrated in the inset. The experiments presented here were conducted in the regions of (sheath-to-sheath)  $L_{\parallel} = 60$  m or  $L_{\parallel} = 105$  m, respectively.

The probe head contained a poloidal array of cylindrical probes which were alternately operated in ion saturation current ( $I_{i,\text{sat}}$ ) and floating potential ( $\Phi_{\text{fl}}$ ) mode. In addition, a triple probe provided electron temperature and density. Further details on the probe head are given in [20]. Probe data for fluctuation analysis was band-pass filtered between 3 kHz and 50 kHz to remove low frequency modes [22] and higher frequency Alfvénic activity, which is often seen in W7-X [23] and can be particularly prominent in the SOL [24].

Turbulence properties can be extracted from a set of one central  $I_{i,\text{sat}}$  probe pin and two poloidally adjacent  $\Phi_{\text{fl}}$  probe pins which are separated by the distance  $d_{1,2}$ . The radial velocity of turbulent structures is then inferred from  $E_{\text{pol}} = (\Phi_{\text{fl},1} - \Phi_{\text{fl},2})/d_{1,2}$  as  $v_r = E_{\text{pol}} \times B_{\text{tor}}/B_{\text{tor}}^2$ . To extract the large-scale fluctuation events, conditional averaging (CA) was employed [3, 7, 9, 10]. The trigger condition for an event is set to two times the standard deviation of the ion saturation current signal.

To ensure good statistics, only time series of at least 300 ms duration were used for the CA analysis, which typically yield several hundreds of events for averaging. In each such time interval, the probe remained at a constant position in

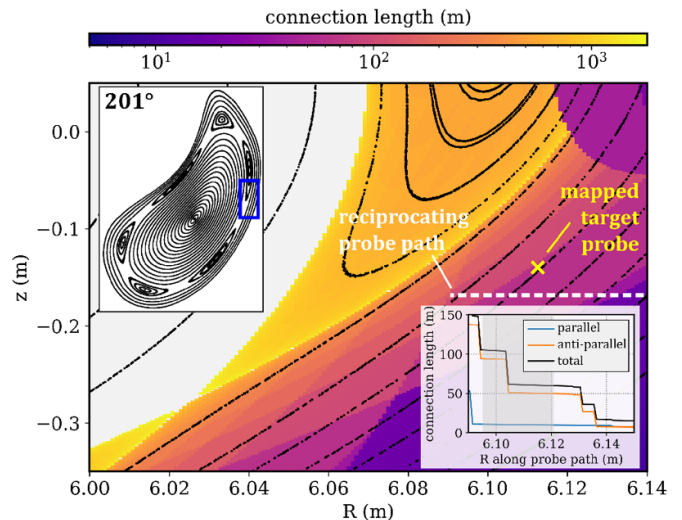


**Figure 1.** Poincaré plot (black dots) and connection length (color coded) in the vicinity of the reciprocating probe path (white, dashed line). Regions of closed field lines are represented by light grey color. Connection length is computed as the sum of partial connection lengths parallel and anti-parallel to the magnetic field. The insets show the full plasma cross section with the region of interest indicated by the blue rectangle (top left) and a profile of connection lengths along the probe path (bottom right). There, the shaded area indicates the probed region for the results presented here. The yellow cross represents the positions of one divertor probe traced along the magnetic field to the poloidal plane of the reciprocating probe measurements.

the SOL and plasma conditions were stationary. In total, 46 sufficiently long datasets with different combinations of electron cyclotron resonance heating (ECRH) power, line integrated plasma density and probe positions are available from otherwise identical experiments. Typical CA results of density and radial velocity based on the detection of positive density events are presented in figure 2 a,b) and show a localized structure with a typical temporal width of  $15 \mu\text{s}$ . The structure is approximately in phase between  $n$  and  $v_r$ , as expected in the typical interchange picture [1, 3, 4]. To illustrate the robustness of this general qualitative behavior and provide examples for the quantitative variability, three data sets are shown in figure 2 a,b) which correspond to different ECRH power levels, while the probe position and average plasma density were similar. The general behavior of a simultaneous density and positive radial velocity peak holds for all three (and all other) measurements, and the density perturbation strength and radial velocity increase only slightly for higher heating power. At the same time, the density base line before and after the turbulent event reveals a somewhat stronger dependence towards higher densities at higher heating power as was reported previously [20].

In addition to the density perturbation, turbulent filaments are known to also feature electron temperature fluctuations [3, 25–27], which may significantly affect the validity of inferring the plasma potential from floating potential measurements. To estimate the role of  $T_e$  fluctuations in our experiments, CA triggered by density events has also been applied to the  $T_e$  signal from a simultaneously operated triple Langmuir

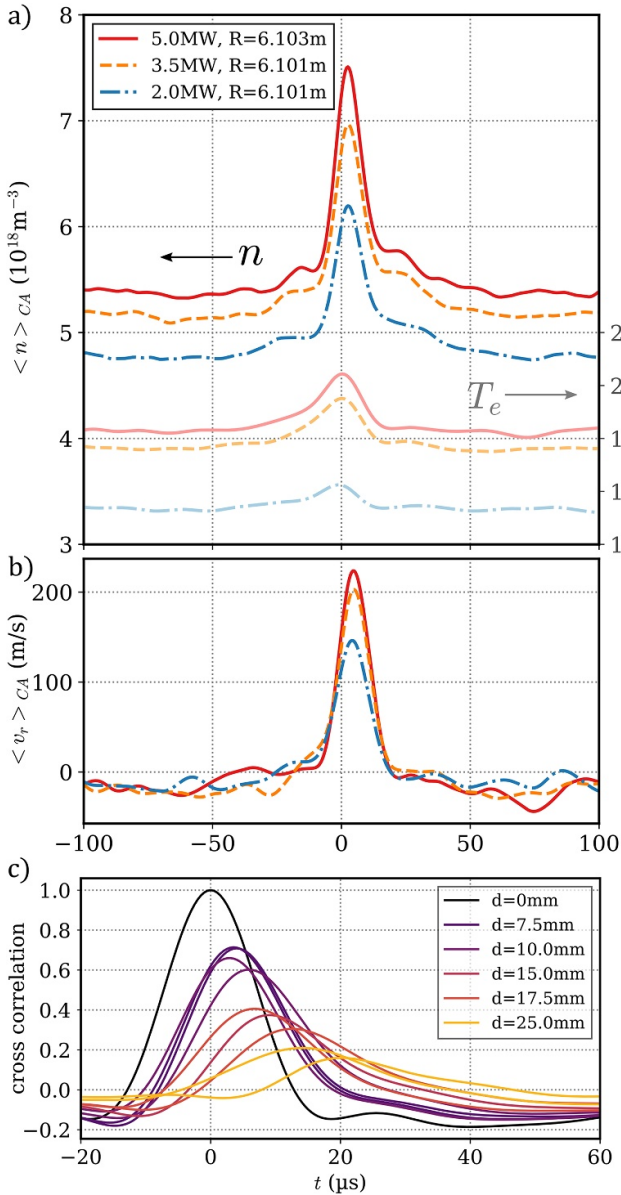


**Figure 2.** Examples of a) density and b) radial velocity from conditional averaging over 400 ms of data, triggered on density fluctuations. In addition, the conditionally averaged electron temperature from a triple probe is represented by lighter colors in a). The three datasets correspond to different ECRH power levels, while the probe position and line averaged plasma density ( $\sim 3 \cdot 10^{19} \text{ m}^{-3}$ ) were kept constant. c) Cross correlation between various poloidally-separated floating potential pins, yielding an upwards-directed propagation velocity of 1.2 km/s and a life-time of 11  $\mu\text{s}$ . The filament size is estimated from the poloidal velocity obtained in c) and the temporal filament width indicated in a).

probe (see probe head layout in [20]). We find typical  $T_e$  fluctuations around 10% of the time-averaged electron temperature as indicated by the representative results in figure 2 a), which are approximately in phase with the density peak. Applying a correction of  $\sim 2.8T_e$  to the floating potential measurements results in the radial velocity becoming a few 10% larger than without the correction, but an exact treatment is difficult and remains outside the scope of this work for now. For the sake

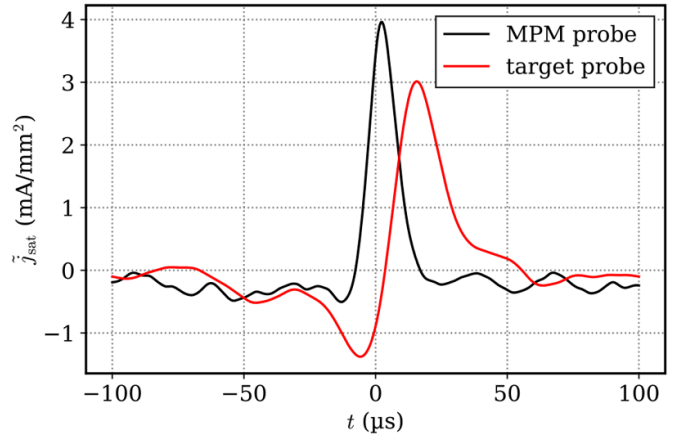


**Figure 3.** Conditionally averaged ion saturation current densities for MPM probe and target probe based on events in MPM data. The mapped position of the target probe to the MPM plane (see figure 1) is displaced about 2 cm poloidally and 1 cm radially from the MPM probe.

of a clear line of arguments in this paper, we will for now neglect  $T_e$  fluctuations for the further analysis and discuss their potential implications in the final section of the paper.

Besides the density fluctuation amplitude and radial velocity provided by the analysis described above, the spatial scale of fluctuation is a fundamental parameter for their dynamics [1]. In the experiment, the (poloidal) size is estimated from the poloidal propagation velocity  $v_{\text{pol}}$  and the temporal width  $\tau_{1/e}$  of the CA analysis assuming a linear propagation as  $\delta_{\perp} = v_{\text{pol}}\tau_{1/e}$ . The temporal width of the structure  $\tau_{1/e}$  is determined from the 1/e width of the density peaks, c.f. Figure 2(a). The poloidal velocity is obtained from a time delay analysis of plasma fluctuations propagating over different poloidally spaced pins on the probe head [20]. The procedure is illustrated by an example data set in figure 2(c), where the cross correlation between different floating potential pins [20] on the probe is shown. Larger poloidal pin distances are represented by lighter colors, while the black curve at  $d = 0$  mm represents the auto-correlation function of one floating potential pin. Besides the increasing time delay between correlation maxima for larger pin separation, the correlation amplitude is seen to decrease quickly, indicating that the life time of the turbulent structures is not much larger than the auto correlation width. Therefore, an elliptical model is employed to properly estimate the poloidal propagation velocity [28–30], yielding an upwards directed velocity which in figure 2(c) is 1.2 km/s. Poloidal velocities obtained in this way are generally comparable to (although systematically slightly smaller than) velocities estimated via  $v_{\text{pol}} = (E_r \times B)/B^2$  where the radial electric field  $E_r$  is determined from the radial profiles of electron temperature  $T_e$  and floating potential  $\Phi_{\text{fl}}$  which were also taken with the reciprocating probe head via  $E_r = -\nabla(\Phi_{\text{fl}} + 2.8T_e)$ . The radial size of the fluctuating structures is not accessible in our experiments. Therefore, the impact of their ellipticity is explored numerically and represented by the error bars of the simulation results in figure 5.

We finally note that these measurements were taken with a poloidal probe array at one specific toroidal position. To prove the filamentary character, i.e. the elongation of fluctuations parallel to the magnetic field, we exploit the magnetic connection to one of the target Langmuir probes. The position of the field line starting from the target probe (probe 12 in divertor module 51) and followed  $\sim 10$  m along (anti-parallel to) the magnetic field to the MPM plane is indicated by the yellow cross in figure 1a). In figure 3, the CA results of both this target probe and a probe on the MPM (pin 17 [20]) is shown. Both probes were operated in ion saturation current mode and the CA was triggered on the MPM probe signal. The target probe result clearly shows an event about 13  $\mu$ s after the event at the MPM. This time delay is approximately consistent with the poloidal distance of 2 cm between MPM probe and mapped target probe and the poloidal filament velocity of 2 km/s, which would result in an expected delay of 2 cm/2 km/s = 10  $\mu$ s. The slightly smaller amplitude and larger temporal width of the event at the target is likely due to the imperfect coherence of the fluctuation along the magnetic field. A more detailed analysis of the correlation of fluctuations between magnetically connected probes at different toroidal positions will be presented in a future publication.

## 2.2. The Hermes model

The simulations used in this work are carried out using the Hermes model implemented in the BOUT++ framework [31–33]. Hermes is a non-isothermal fluid turbulence model which evolves the full density profile. In this work, simulations are performed only in the drift plane, and therefore parallel terms have been neglected, and parallel effects must be included in the closure terms. The equations solved here evolve plasma density  $n$ , electron pressure  $p_e$ , and vorticity  $\omega$ . The full drift-plane model is as follows:

$$\frac{\partial n}{\partial t} = -\nabla \cdot (n\mathbf{V}_{E \times B} + n\mathbf{V}_{mag}) \quad (1)$$

$$\begin{aligned} \frac{3}{2} \frac{\partial p_e}{\partial t} = & -\nabla \cdot \left( \frac{3}{2} p_e \mathbf{V}_{E \times B} + \frac{5}{2} p_e \mathbf{V}_{mag} \right) \\ & - p_e \nabla \cdot \mathbf{V}_{E \times B} \end{aligned} \quad (2)$$

$$\begin{aligned} \frac{\partial \omega}{\partial t} = & -\nabla \cdot (\omega \mathbf{V}_{E \times B}) - \nabla \cdot (en\mathbf{V}_{mag}) \\ & + \nabla \cdot (\mu_i \nabla_{\perp} \omega) \end{aligned} \quad (3)$$

where  $\mu_i$  is the ion viscosity coefficient as defined in [34].

The  $\mathbf{E} \times \mathbf{B}$  and magnetic drifts are given by:

$$\mathbf{V}_{E \times B} = \frac{\mathbf{b} \times \nabla \phi}{B} \quad \mathbf{V}_{mag} = -\frac{T_e}{e} \nabla \times \frac{\mathbf{b}}{B} \quad (4)$$

where  $T_e$  is given in eV. All simulations presented here employ the Boussinesq approximation [35] (although this is not required in Hermes), and therefore the vorticity is described by:

$$\omega \approx \nabla \cdot \left( \frac{en_0}{\Omega_i B} \nabla_{\perp} \phi \right) \quad (5)$$

where  $\Omega_i = eB/m_i$  is the ion cyclotron frequency. As the plasma model is cast in conservative form, it conserves particle number and an energy:

$$E = \int dv \left( \frac{1}{2} \frac{ne^2}{\Omega_i} |\nabla \phi|^2 + \frac{3}{2} p_e \right) \quad (6)$$

where the terms correspond to the ion  $\mathbf{E} \times \mathbf{B}$  energy and the electron thermal energy. Differential operators are discretised using flux-conservative finite volume methods, which are discussed in Reference [32].

Parallel closures for 2D simulations are of paramount importance to the simulations presented here. Hermes includes closures to facilitate realistic drift plane simulations. For SOL simulations, sheath closures are available which add the following terms to the respective equations:

$$\frac{\partial n}{\partial t} = \dots - \frac{\sqrt{T_i/m_i}}{2L_{\parallel}} n \quad (7)$$

$$\frac{\partial p_e}{\partial t} = \dots - T_e \frac{\sqrt{T_i/m_i}}{2L_{\parallel}} n \quad (8)$$

$$\frac{\partial \omega}{\partial t} = \dots + \frac{enc_s}{L_{\parallel}} \left[ 1 - \sqrt{\frac{m_i}{4\pi m_e}} \exp(-e\phi/T_e) \right] \quad (9)$$

where  $c_s = \sqrt{T_e/m_i}$  is the sound speed.

## 3. Results, filament scaling

Plasma filaments are advected by  $\mathbf{E} \times \mathbf{B}$  effects due to charge separation arising from diamagnetic drifts. The resulting transport is determined by the mechanism mitigating the charge separation. Filaments with a short connection length ( $L_{\parallel}$ ) to the sheath resolve charge separation via parallel currents, but if the connection length is long enough (or the filament small enough) the charge can be short-circuited via perpendicular currents. This distinction of sheath- vs inertially-limited filaments is often visualized by employing a scaling of filament velocity as a function of perpendicular filament size,  $\delta_{\perp}$  [1, 36, 37]. A large, sheath-limited filament will have a velocity which scales as the  $\delta_{\perp}^{-2}$ , whereas inertially limited filaments scale as  $\delta_{\perp}^{1/2}$ . A very thorough discussion of filament propagation and scalings can be found in [1, 12].

### 3.1. Experimental scaling results

Based on the methods and data sets described in section 2, a scatter plot of the radial filament velocities as a function of their size is presented in figure 4(a). The observed filaments have sizes  $\delta_{\perp}$  between a few mm and 30 mm. The highest radial velocities of up to 300 m s<sup>-1</sup> are found at medium-sized filaments of around 10 mm. The time-averaged electron temperature  $T_e$  is color coded to illustrate the fact that the experimental conditions can vary significantly between individual data points. For the sake of visual clarity, error bars are omitted here but are later shown in figure 5.

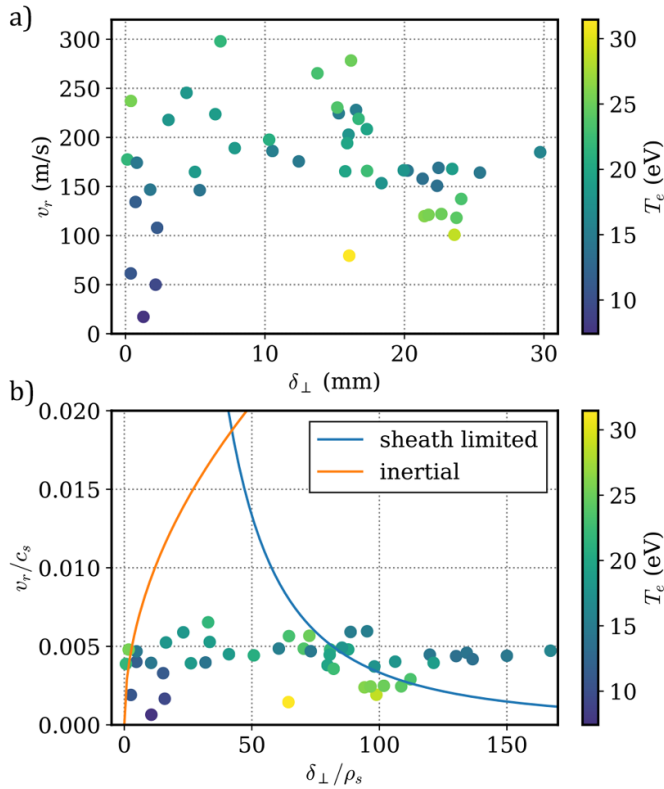


**Figure 4.** Experimentally determined filament properties in absolute (a) and normalized (b) units. Each symbol represents the conditionally averaged result of a 300 ms time series. The fundamental scaling laws are shown as solid lines.

To discuss filament scalings, it is more convenient to display their properties as normalized quantities [1, 36, 37]. Such a normalized scaling is presented in figure 4(b), where the filament velocity is normalized to the local sound speed  $c_s = \sqrt{T_e/m_i}$  and the size is normalized to the drift scale  $\rho_s = m_i c_s / (eB)$ . In addition, the fundamental scaling laws [1, 37] for the sheath-limited regime

$$v_{\text{SL}} = c_s \left( \frac{L_{\parallel}}{R} \right) \left( \frac{\rho_s}{\delta_{\perp}} \right)^2 \quad (10)$$

and the inertial regime

$$v_{\text{IN}} = c_s \sqrt{\alpha \delta_{\perp} / R} \quad (11)$$

are superimposed as solid lines. Here, typical values for our experiments in W7-X have been used:  $\rho_s = 0.2$  mm, relative density fluctuation amplitude  $\alpha = \tilde{n}/n_0 = 0.3$ , curvature radius  $R = 6$  m, and connection length  $L_{\parallel} = 100$  m. The experimentally observed velocities are well below the inertial scaling and, for smaller filaments, also well below the sheath-limited scaling. Only for larger filaments ( $\delta_{\perp}/\rho_s > 70$ ), the experimental data is in a similar range as the sheath-limited scaling. Comparing the data in figure 4(b) to the radial velocity of similar filament sizes in tokamaks [1], we find that the velocities are much slower in W7-X. As an example, the normalized velocity for  $\delta_{\perp}/\rho_s = 100$  is one order of magnitude slower in W7-X compared to ASDEX Upgrade [37].

### 3.2. 2D simulations

Simulations were performed using the drift-plane approximation such that all parameters (and geometry) are constant in the parallel direction. Initial conditions were motivated by the typical filament parameters observed by the reciprocating probes. The simulations were initialized as a circular Gaussian cross-section, with a 30% density perturbation above the time averaged density  $n_0 = 6 \cdot 10^{18} \text{ m}^{-3}$  at a time averaged temperature of  $T_{e,0} = 22$  eV. Both filaments with an initially unperturbed temperature as well as with a 10%  $T_e$  perturbation above the background have been investigated numerically.

The experimental data presented here was obtained in two different connection length regimes, approximately 105 m and 60 m, see figure 1. As the region with 105 m connection length is closer to the separatrix, filaments in this region tend to be hotter and have stronger density perturbations. Background densities are also much higher for these filaments. Due to the difficulty in disentangling these experimental parameters, and as  $L_{\parallel}$  is of paramount importance in 2D closures, we present here the filament scaling as a function of poloidal filament diameter ( $\delta_{\perp}$ ) as seen both in experiment and simulation for the two different  $L_{\parallel}$  regimes, figure 5. The scattered data points are the same as in figure 4(a) but distinguished by connection length into the two subfigures. While the size distribution is similar in both cases, higher velocities are seen in the 105 m case. This is in agreement with the dedicated simulations for each  $L_{\parallel}$  case, which also show similar qualitative trends but higher velocities at  $L_{\parallel} = 105$  m, as well as with the analytical sheath limited scaling calculated according to equation (10).

The experimental measurements presented are limited to determining the poloidal size of any radial filament size. The shaded regions around the simulation results in figure 5 correspond to the maximum and minimum  $v_{\text{max}}$  achieved when varying the filament ellipticity—although this does not scale monotonically—while keeping the poloidal size  $\delta_{\perp}$  fixed. The maximum filament velocity corresponds to an elliptical filament whose major axis is poloidally-aligned, and the minimum velocity is a filament where the major axis is aligned in the radial direction. Both cases are for a major axis which is four times the minor axis of the elliptical filament. For a much more detailed discussion on the effects of filament ellipticity in the drift plane, see Reference [38]. As shown by the error bars in figure 5, the uncertainty from the unknown filament ellipticity has no major role for the agreement between experiment and simulation.

The experimental error bars correspond to typical errors of 30% in the size estimation and 40% in the velocity estimation, which include both statistical errors in the experimental data and systematic errors due to the geometric alignment of probe pins with respect to the filament. To assess the latter, a synthetic probe diagnostic has been developed for the simulated filaments, providing an assessment of the underestimation of filament size due to the fact that probe will not always measure a filament at its largest diameter.

Given the uncertainties and simplifications in both experiment and simulation, the agreement between them is surprisingly good. The fact that the experiments in figure 5 agree

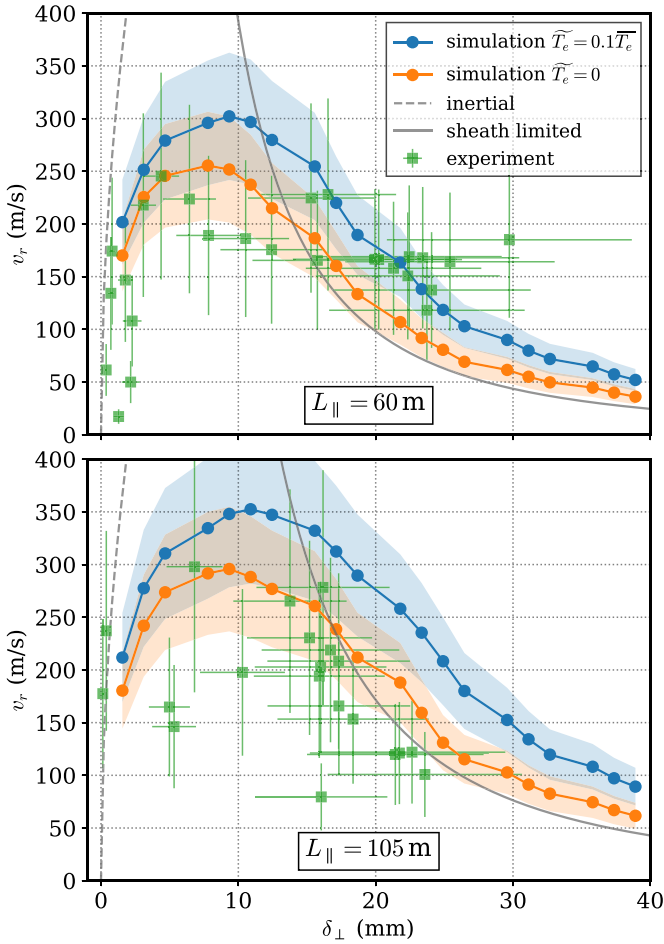


**Figure 5.** Comparison of filament scaling in experiment and simulation. The experimental data points were distinguished by connection length and simulations were performed for each connection length separately. The shaded region around the simulations results represents the uncertainty due to perpendicular filament ellipticity.

better with the simulations without initial  $T_e$  perturbation is not surprising since this was also the assumption for the interpretation of experimental data, see section 2. The simulations including an initial 10%  $T_e$  perturbation of the filament result in 20%-50% higher radial velocity. A similar correction towards higher  $v_r$  can be expected for the experimental results when the 10%  $T_e$  perturbation is included in the calculation of  $v_r$  from the plasma potential signals. However, no such data set for the experiments is shown here since the exact nature of the correction still remains to be addressed in future, detailed investigations.

Concluding this comparison, the agreement between experiment and simulation in figure 5 is robust to changes in the initial conditions for the simulated filaments, for instance the range of temperatures shown in figure 4. One can therefore determine that despite the complex geometry and large range of experimental parameters, the filaments seen in the SOL of W7-X exhibit a radial propagation in agreement with simulation.

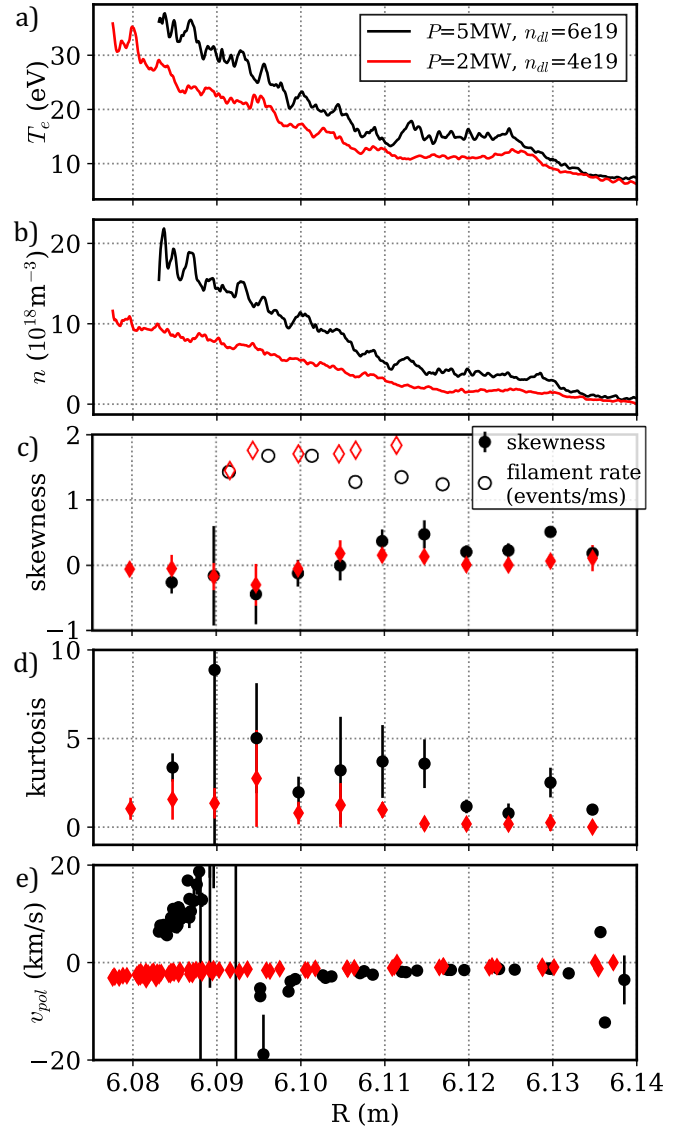


**Figure 6.** Profiles taken with the reciprocating probe for two different plasma scenarios. In both scenarios, the averaged results of three identical fast plunges are shown. The skewness and kurtosis (c,d) were determined from the probability distribution functions of ions saturation current fluctuations where the kurtosis is defined such that a normal distribution has kurtosis = 0. The error bars indicate the scatter between the six data sets (three plunges, each inwards and outwards). The poloidal velocity of fluctuations (e) is estimated from cross correlation time delay analysis across the probe array [20]. The horizontal axis shows the probe position in cylindrical co-ordinates along the probe path, see figure 1.

### 3.3. Discussion, implications for SOL transport

The slow radial propagation of filaments in W7-X implies that a filament only moves sub-cm distances during its lifetime which is typically no more than a few  $10 \mu\text{s}$ . Therefore, filaments cause only local perpendicular transport. This is in contrast to tokamaks, where filaments can propagate over significantly larger radial distances, thereby transporting hotter and denser plasma from the separatrix into the far SOL [6]. There, this process manifests in strongly positive skewness

and kurtosis of density fluctuations in the far SOL, indicating the presence of strong positive density perturbations in a rather quiet background plasma [1, 3, 5, 39]. In W7-X, the situation is different, as further illustrated by the skewness and kurtosis profiles in figure 6. The entire radial range probed by the fast plunges of the manipulator is shown (in contrast to the probe remaining at intermediate constant positions for the CA analysis, which for the experiments shown above between 6.095 m and 6.120 m). In addition to the statistical parameters, the electron temperature and density profiles are shown, as well as the poloidal propagation velocity of fluctuations along the probe array [20]. To illustrate the role of plasma conditions, two different scenarios are shown: high ECRH power (5MW) at higher density (line integrated density  $6 \cdot 10^{19} \text{ m}^{-2}$ ) in black, and low ECRH power (2MW) at medium density ( $4 \cdot 10^{19} \text{ m}^{-2}$ ) in red. For each scenario, the data was averaged over three independent measurements in separate discharges, which are well reproducible in W7-X. The skewness profiles are rather flat across the entire probed region, indicating a similar occurrence of positive and negative density events. The kurtosis profiles show more variation, but are notably flat in the far SOL, further supporting the conclusion that the turbulent structures seen far from the separatrix are a part of the (approximately normal distributed) background turbulence and have *not* been advected there from a different radial position (e.g. the separatrix in case of tokamaks). The larger kurtosis values with larger error bars (representing scatter between the different data sets) in the 5MW scenario around  $R = 6.09$  m coincide with the observation of a poloidal velocity shear layer at this position. The occurrence of this shear layer is well reproducible [20] but not yet understood, since it is well outside the expected separatrix position, which is around  $R = 6.05$  m. Nevertheless, we emphasize that the filaments measured by the probe outside of this region have not (predominantly) originated at this shear layer, since a) the shear layer is only seen at higher heating powers and higher densities, and b) the radial velocities and statistical profiles in figure 6 do not support such a statement. The conclusion that filaments are created locally everywhere along our measurement range is further supported by the filament detection rate represented by the open symbols in figure 6 c), which reveals a similar filament occurrence in the positions investigated by CA. Regardless of the shear layer, the poloidal velocities are typically in the range of a few km/s and therefore one order of magnitude larger than the radial filament velocities. The fast poloidal propagation of filaments is furthermore reflected by the rather symmetric shape of the filament signals in figures 2, 3, which is again in contrast to many observations in tokamaks, where due to the faster radial propagation the filaments seen by probes are characterized by a steep front and a longer tail [1].

Finally, the question of the role of  $T_e$  fluctuations needs to be addressed. As shown in figure 1 c), small yet significant  $T_e$  fluctuations have been observed in phase with the filament density peak. While it has been shown in certain situations in tokamaks this can strongly affect conclusions made from floating potential measurements, [26, 27], the implications in the W7-X experiments are not as grave. Depending on the

exact treatment of the corrections, the true radial filament velocity might be on the order of 10% (upper limit: 50%) higher than in the experimental data shown in figures 4 and 5, which would also agree with the role of such  $T_e$  perturbations seen by the simulations. A more accurate conclusion requires additional experiments and work beyond the scope of this paper. However, even in the most extreme error situation of a systematically up to 50% higher radial filament velocity (which is almost within the 40% error bars in figure 5), the main message remains valid: The filaments observed in the W7-X SOL are so slow that their radial displacement during their life-time is smaller than their own size.

#### 4. Conclusion

Filaments have been investigated in the SOL of W7-X (outside of magnetic islands) where they have been identified and characterized by probe measurements. The presence of filaments was not clear to begin with, as the curvature drive varies greatly along a field line in the W7-X SOL. Approximating the net drive on the filament using field-line-averaged curvature [19] in 2D yields good agreement of the filament scaling between experiment and simulation. It is found that filaments in W7-X exhibit slow radial motion, while their poloidal velocity induced from the radial electric field is much larger than the radial velocity. The simulations reproduce this observation and indicate the large major radius—and therefore small normal magnetic curvature—of W7-X as the primary cause.

These observations imply that radial propagation of turbulent filaments is not a major contribution for the perpendicular transport in the W7-X SOL, as the filaments do not move significant radial distances within their life time and only result in local transport on the scale of their own size. Following the common definition of *blobs* [1], the filaments in W7-X therefore cannot be described as blobs. The flat skewness and kurtosis profiles in the far SOL support that the filaments are radially essentially bound to a flux surface. In particular, ballistic radial motion of filaments and radial turbulence spreading [6] is not observed.

A quantitative assessment of the role of filamentary transport for the entire W7-X SOL requires a full three-dimensional treatment. In particular, role of filaments in magnetic islands needs to be assessed, since the islands are the essential part of the W7-X island divertor and have been shown to feature additional plasma dynamics [15, 20, 40], adding to the complexity of the filament analysis. Therefore, future work should include the full magnetic geometry.

#### Acknowledgments

The authors would like to acknowledge the work of the BOUT++ development team. BOUT++ is an open-source framework available at [boutproject.github.io](https://github.com/boutproject/bout). Furthermore, the authors would like to thank Golo Fuchert and Ben Dudson for many fruitful discussions. This work has been carried out within the framework of the EUROfusion Consortium and

has received funding from the Euratom research and training programme 2014-2018 and 2019-2020 under grant agreement No 633053. The views and opinions expressed herein do not necessarily reflect those of the European Commission

## ORCID iDs

Carsten Killer  <https://orcid.org/0000-0001-7747-3066>

Brendan Shanahan  <https://orcid.org/0000-0002-8766-8542>

Michael Endler  <https://orcid.org/0000-0003-2314-8393>

Kenneth Hammond  <https://orcid.org/0000-0002-1104-4434>

Lukas Rudischhauser  <https://orcid.org/0000-0002-3696-7067>

## References

- [1] D'Ippolito D A, Myra J R and Zweben S J 2011 *Phys. Plasmas* **18** 060501
- [2] Endler M, Niedermeyer H, Giannone L, Holzhauser E, Rudyj A, Theimer G and Tsois N 1995 *Nucl. Fusion* **35** 1307
- [3] Boedo J A *et al* 2001 *Phys. Plasmas* **8** 4826
- [4] Grulke O, Terry J L, LaBombard B and Zweben S J 2006 *Phys. Plasmas* **13** 012306
- [5] Nold B, Conway G D, Happel T, Müller H W, Ramisch M, Rohde V, Stroth U and the ASDEX Upgrade Team 2010 *Plasma Phys. Control. Fusion* **52** 065005
- [6] Manz P *et al* 2015 *Phys. Plasmas* **22** 022308
- [7] Grulke O, Klinger T, Endler M and Piel A 2001 *Phys. Plasmas* **8** 5171
- [8] Antar G, Krasheninnikov S, Devynck P, Doerner R, Hollmann E, Boedo J, Luckhardt S and Conn R 2001 *Phys. Rev. Lett.* **87** 065001
- [9] Carter T A 2006 *Phys. Plasmas* **13** 010701
- [10] Happel T, Greiner F, Mahdizadeh N, Nold B, Ramisch M and Stroth U 2009 *Phys. Rev. Lett.* **102** 255001
- [11] Fuchert G, Birkenmeier G, Ramisch M and Stroth U 2016 *Plasma Phys. Control. Fusion* **58** 054005
- [12] Myra J R, Russell D A and D'Ippolito D A 2006 *Phys. Plasmas* **13** 112502
- [13] Krasheninnikov S I, D'Ippolito D A and Myra J R 2008 *J. Plasma Phys.* **74** 679
- [14] Kocsis G *et al* 2017 *44th Conf. on Plasma Physics*
- [15] Zolotnik S *et al* 2019 *Plasma Phys. Control. Fusion* **62** 014017
- [16] Pedersen T S, Otte M, Lazerson S, Helander P, Bozhakov S, Biedermann C, Klinger T, Wolf R C Bosch H S *et al* 2016 *Nat. Commun.* **7** 13493
- [17] König R *et al* 2002 *Plasma Phys. Control. Fusion* **44** 2365
- [18] Shanahan B, Dudson B and Hill P 2018 *Plasma Phys. Control. Fusion* **61** 025007
- [19] Shanahan B, Dudson B and Hill P 2018 *Journal of Physics: Conf. Series* **1125** 012018
- [20] Killer C *et al* 2019 *Nucl. Fusion* **59** 086013
- [21] Hammond K C *et al* 2019 *Plasma Phys. Control. Fusion* **61** 125001
- [22] Ballinger S *et al* 2018 *Nuclear Mater. Energy* **17** 269
- [23] Rahbarnia K *et al* 2019 *46th Conf. on Plasma Physics* European Physical Society
- [24] Liu S C *et al* 2018 *Phys. Plasmas* **25** 072502
- [25] Hidalgo C *et al* 1996 *Contrib. Plasma Phys.* **36** 139
- [26] Gennrich F P and Kendl A 2011 *Plasma Phys. Control. Fusion* **54** 015012
- [27] Nold B, Ribeiro T T, Ramisch M, Huang Z, Müller H W, Scott B D and Stroth U 2012 *New J. Phys.* **14** 063022
- [28] Briggs B H, Phillips G J and Shinn D H 1950 *Proc. Phys. Soc. B* **63** 106
- [29] Bleuel J, Endler M, Niedermeyer H, Schubert M, Thomsen H and Team T W-A 2002 *New J. Phys.* **4** 38
- [30] Prisiazhniuk D, Krämer-Flecken A, Conway G D, Happel T, Lebschy A, Manz P, Nikolaeva V and Stroth U 2017 *Plasma Phys. Control. Fusion* **59** 025013
- [31] Dudson B D, Umansky M V, Xu X Q, Snyder P B and Wilson H R 2009 *Comput. Phys. Commun.* **180** 1467
- [32] Dudson B D and Leddy J 2017 *Plasma Phys. Control. Fusion* **59** 054010
- [33] Leddy J, Dudson B and Willett H 2017 *Nucl. Mater. Energy* **12** 994
- [34] Madsen J, Naulin V, Nielsen A H and Rasmussen J J 2016 *Phys. Plasmas* **23** 032306
- [35] Gray D D and Giorgini A 1976 *Int. J. Heat Mass Trans.* **19** 545
- [36] Theiler C, Furno I, Ricci P, Fasoli A, Labit B, Müller S H and Plyushchev G 2009 *Phys. Rev. Lett.* **103** 065001
- [37] Carralero D *et al* 2015 *Rev. Lett.* **115** 215002
- [38] Omotani J T, Militello F, Easy L and Walkden N R 2016 *Plasma Phys. Control. Fusion* **58** 014030
- [39] Labit B *et al* 2007 *Plasma Phys. Control. Fusion* **49** B281
- [40] Liu S *et al* 2019 *Nucl. Fusion* **59** 066001